Supplement to: **Using highly time-resolved online mass spectrometry to examine biogenic and anthropogenic contributions to organic aerosol in Beijing** by Mehra, Archit et al.

1. Measurements

1.1. FIGAERO-CIMS

A ToF-CIMS using an iodide ionisation system was coupled to a FIGAERO, first designed by Lopez-Hilfiker et al (2014) [1]. The specific Aerodyne FIGAERO design used in this study was recently described in Bannan et al., 2019. This inlet enables near-simultaneous detection of gas and aerosol phase composition. For clarity, aerosol phase measurements will be referred to as FIGAERO-CIMS and gas-phase as I-CIMS, herein.

The aerosol was sampled through a 5 metre stainless steel inlet at a flow rate of 30 standard litres per minute (SLM) fitted with a 3.5 µm cyclone, for removal of larger particles. Particles were subsampled from the inlet using a 0.1 m stainless steel line at a flow rate of 2 SLM and collected on a polytetrafluoroethylene (PTFE) filter (2 µm pore size, Zeflour™, Pall Corporation) in the FIGAERO inlet for the duration of gas phase measurement, 45 minutes in this case. Following this, the particles were desorbed by flowing heated nitrogen through the filter. The desorption cycle consisted of a 15-minute temperature ramp to a filter temperature of ~ 200 °C, 15-minutes held at that temperature and a 10-minute cool back to container temperature (~ 25 °C).

The detailed gas phase sampling setup is described in Zhou *et al.* (2018). Briefly, the reagent ion was produced from gas mixtures of CH_3I which were ionized by flowing through a Tofwerk X-ray ionization source. This flow enters an ion molecule reaction region (IMR) where it mixes with the analyte and adducts are formed and taken into the mass spectrometer. Instrument, filter and gas-phase backgrounds were taken throughout the measurement period alongside field calibrations of formic acid which were used to ensure a constant instrument sensitivity across the campaign.

This paper focuses on the results from the FIGAERO-CIMS, with other co-located measurements utilised to frame the discussion and for interpretation of factors. These include meteorological measurements taken from the IAP tower, measurements of trace gases such as NO_x, SO_2 and O_3, radicals such as OH, RO_2 [3] and NO_3 alongside VOCs measured by proton transfer reaction mass spectrometry (PTR-MS) [4] and gas chromatography with flame ionisation detection (GC-FID) and aerosol measurements by AMS, SMPS and Orbitrap UPLC-MS.

1.2. Co-located Measurements

1.2.1. FAGE

Radical measurements were made from the University of Leeds FAGE instrument [5]. Two detection cells, the HOx cell and the ROxLIF cell, were located on the roof container at a sampling height of approximately 3.5 m. Sequential measurements of OH and HO_2 were made in the HOx cell, whilst sequential measurements of total RO_2 and HO_2 + RO_2-complex were made in the ROxLIF cell[6]. Here, RO_2-complex refers to any RO_2 species (primarily those derived from alkene and aromatic hydrocarbons) that have the potential to decompose into OH in the presence of NO on the time-scale of the FAGE cell residence time. By subtraction of RO_2-complex from total RO_2, the concentration of RO_2 species that do not decompose to OH in the presence of NO in the FAGE cell (RO_2-simple) was derived.

For the entire campaign, the HOx cell was equipped with an inlet pre injector (IPI) which chemically scavenged ambient OH by periodically injecting propane into the air stream just above the FAGE inlet to determine the background signal contribution from solar scatter, laser scatter and any OH internally generated within the FAGE cell[7].

The instrument was calibrated every few days by over-flowing the detection cell inlet with a turbulent flow of high purity humid air containing a known concentration of OH (and HO_2) radicals generated by photolysing a known concentration of H_2O vapour at 185 nm. For calibration of RO_2 concentrations, methane was added to the humidified air flow in sufficient quantity to convert OH to CH_3O_2. The product of the photon flux at 185 nm and the time spent in the photolysis region was measured before and after the campaign using N_2O actinometry [8].

1.2.2. Trace Gas Measurements

Gas-phase measurements of O_3, NO, NO_2 and SO_2 were made at the IAP site. Instrumentation was housed in a converted shipping containing laboratory and sampled from a shared sample manifold with an elevated inlet at 8 m. NO was measured via the chemiluminescent reaction with O_3 with a Thermo Scientific Model 42i NO_x analyser and NO_2 was measured using a Teledyne Model T500U Cavity Attenuated Phase Shift (CAPS) spectrometer. O_3 was measured using a Thermo Scientific Model 49i UV photometric analyser. SO_2 was measured using a Thermo Scientific 43i fluorescence spectrometer. All instruments were calibrated regularly throughout the measurement period, with a 'zero' or 'background' calibration using a Sofnofil/charcoal trap. Span (high concentration) calibrations were carried out using gas standards. Both the Thermo Scientific 42i and Teledyne Model T500U instrument calibrations are traceable to the National Physical Laboratories (NPL) NO scale.

1.2.3. NO_3

Details about the broadband cavity enhanced absorption spectrometer can be found in Kennedy et al.,(2011) [9]. Briefly, air was heated to 140 °C to thermally dissociate N_2O_5 into NO_3 before it entered the observation cavity. This cavity was formed of two high-reflectivity mirrors with peak R ~ 0.9998-0.9999 in the wavelength region of 640-680 nm. The sum of N_2O_5 and NO_3 was measured by observing the strong optical absorption band of NO_3 in the above wavelength range. Temperature of the cavity was kept at 85±1 °C to prohibit the recombination of NO_3 and NO_2 and to maintain the stability of the optical transmission signal. A very fast flow rate of 20 LPM (litres per minute) was adopted to minimise the residence time of the gas through the tubes which were all made of perfluoroalkoxy alkane polymer. Loss of NO_3 through the system has been characterised to be around 10% as detailed in Kennedy et al., (2011).

Due to the generally high aerosol loading in Beijing which greatly attenuates the intracavity light intensity and thus deteriorates instrument sensitivity, a PTFE filter of pore size 1 mm was used to remove aerosol particles from the air stream. This filter acts also as a point loss (~10%) for NO_3 but incurs negligible loss for N_2O_5 [10]. Due to the typical large prevalence of N_2O_5 over NO_3 (by a factor of >10) during APHH-Beijing, we expect this filter loss to be small for the total sampling of N_2O_5+NO_3. Aging of the filter through accumulation of aerosol particles may potentially introduce larger uncertainties to the transmission efficiency of NO_3 and N_2O_5. If this effect is significant, clear discontinuities should be observable in the N_2O_5+NO_3 time series data, as pointed by Dube et al. (2006). However, we found no such signs throughout the entire campaign.

1.2.4. AMS & SMPS

Aerosol particle composition was measured by Aerodyne high-resolution AMS (HR-AMS hereafter). Briefly, the particles larger than 2.5 µm were filtered out by the $PM_{2.5}$ cyclone firstly, and the remaining fine particles were subsequently dried by a dryer located upstream of the HR-AMS. The dried particles were sampled into the HR-AMS in the end, which was operated in the mass-sensitive V-mode with a time resolution of 5 min. The ionization efficiency (IE) and relative ionization efficiencies (RIEs) were calibrated using pure ammonium nitrate and ammonium sulfate particles. The composition-dependent collection efficiency (CDCE) was applied to the mass loadings of nonrefractory submicron species (organics, sulfate, nitrate, ammonium, and chloride). A detailed description of the AMS measurement and data analysis are given in Xu et al., 2019. [11]

A scanning mobility particle sizer (SMPS) instrument measured particle size distributions (TSI 3080 EC, 3082 long DMA, 3775 CPC, TSI, USA), measuring the range 14–615 nm. [12]

Measurements of aerosol composition with AMS were carried out at the same site during this period, The FIGAERO-CIMS measurements were conducted on an inlet with a 3.5 micron cyclone while AMS measurements were PM_1, thus an exact comparison is not available. The comparison presented in Figure S1 shows that the same general features are consistent between the measurements of FIGAERO-CIMS, AMS and SMPS.

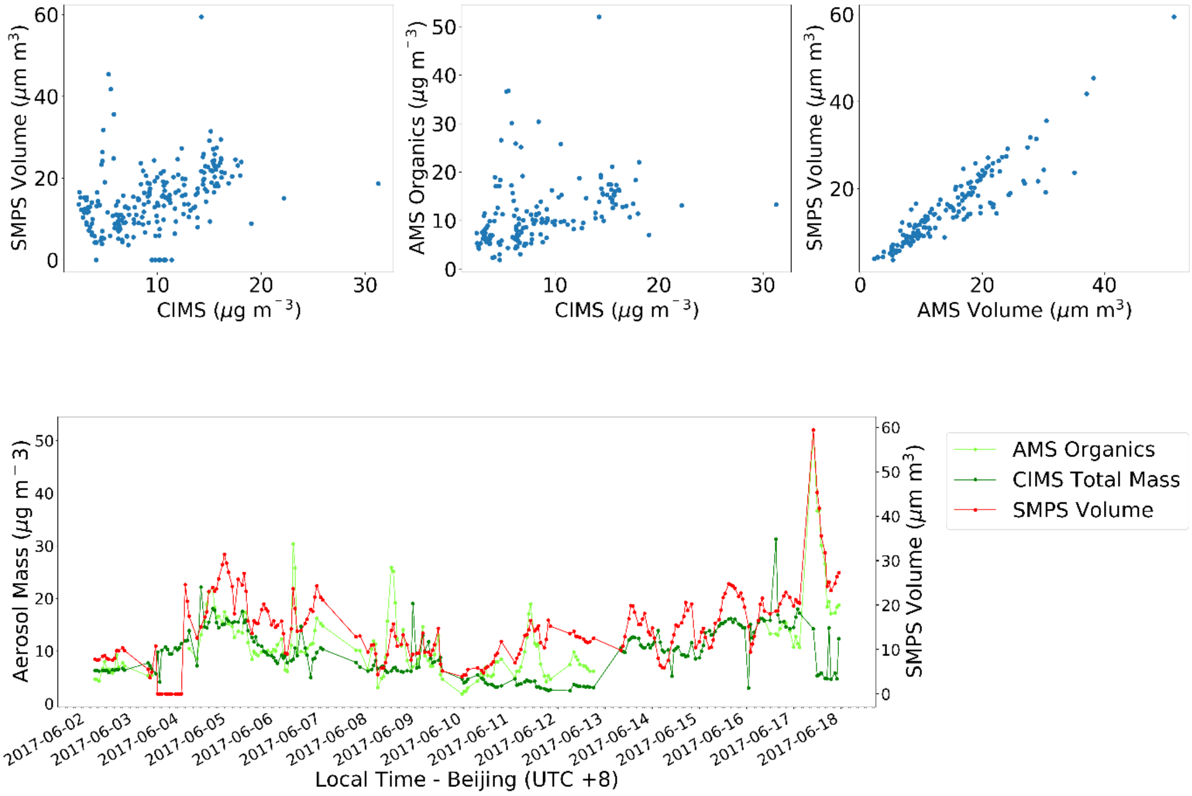

Figure S1 – Comparison of SMPS, AMS and FIGAERO-CIMS Measurements

A PMF analysis was carried out for the AMS analysis and the factors from this are included in this manuscript for comparison with the FIGAERO-CIMS factors.

The FFOA spectrum was characterized by prominent hydrocarbon ion series of $C_nH_{2n-1}^+$ and $C_nH_{2n-1}^+$, consistent with the previously reported reference spectra [8,9]. The tight correlations between FFOA and primary emission species (NO_x and BC, R>0.6) supported that FFOA arose from primary emission sources, rising through the evening and peaking overnight. The mass spectra of COA showed high ratios of m/z 55/57 (2.5), which was comparable with the spectral characteristics of cooking emission [10,11]. The COA tracks well with C6H10O+(R=0.9), a tracer of cooking emission [12]. The diurnal profiles of COA showed pronounced two peaks at ~12:00 and ~20:00, corresponding to the cooking activities. Three SOA factors showed significantly higher O/C ratios (0.67-1.48), and correlated well with SIA (R=0.53-0.7). Compared to LO-OOA and MO-OOA, OPOA showed relatively higher f43 (fraction of m/z 43 in OA). In addition, OPOA showed an elevation during the daytime, peaking at midday and remaining elevated through the afternoon, implying the effect of photochemical processing, which was supported by the tight correlation with O_x (R=0.57), a tracer for the extent of photochemical processing in urban atmosphere [13] . In contrast, LO-OOA showed a sharper peak during the early morning and lower levels in the afternoon and MO-OOA showed a more consistent afternoon peak typical of *in situ* SOA formation.

1.2.5. PTR-MS

VOC mixing ratios were recorded using a Proton Transfer Reaction-Time of Flight-Mass Spectrometer (PTR-TOF-MS; Ionicon Analytik, Innsbruck). The instrument was operated at 5 Hz with the drift tube maintained at 60 °C with a pressure 1.9 mbar and a voltage of 490 V applied across it giving an E/N ratio (where E is electric field strength and N is the buffer gas density) of 130 Td. The instrument subsampled at 30 sccm from a 0.5 inch (O.D.) PFA common inlet line, running from 102 m on the IAP meteorological tower to an air conditioned container at the foot of the tower in which the instrument was situated at a flow rate 90 - 103 L min^{-1}.

The instrument was calibrated twice weekly using a 15 component 1 ± 0.1 ppm VOC standard (National Physical Laboratory, Teddington, UK) dynamically diluted into zero air to provide a 6 point calibration. The PTR-TOF-MS instrumental setup is described in detail by Acton et al. (2020).

1.2.6. GC-FID

VOCs were measured using dual channel gas chromatography (GC) with flame ionisation detection, a detailed description of the set-up can be found in Hopkins *et al.* [19].

1.2.7. UPLC-MS

Aerosol filter samples were collected using an ECOTECH HiVol 3000 (Ecotech, Australia) with a $PM_{2.5}$ selective inlet at a flow rate of 1.33 m^3 min^{-1}. The samples were taken at the Institute of Atmospheric Physics in Beijing, China, between the 18th May and 24th June 2017. The water-soluble fraction of the aerosol was extracted from a small cutting of the filter sample (~64.5 cm^2). Initially the filter sample was cut into 1 cm^2 pieces and left in 4mL LC-MS grade for 2 hours in the dark. The samples were then sonicated for 30 minutes. The water extract was then pushed through a 0.22 µm filter. An additional 1 mL of water was then added to the filter pieces and extracted through the 0.22 µm filter and combined with the previous extract. This combined extract was then reduced to dryness using a Biotage solvent evaporator, before being reconstituted in 50:50 H_2O:MeOH. The sample was then analysed using Ultra-high-performance liquid chromatography tandem mass spectrometry (UHPLC-MS^2), more details for the analysis can be found in Bryant et al. [20].

1.3. Data Processing and Analysis

Data from the mass spectrometer was saved at 1Hz time resolution and analysed using Tofware (v.3.1.0, Aerodyne Research Inc., Billerica, MA and Tofwerk AG, Thun, Switzerland) in Igor Pro (v7, Wavemetrics, Portland, OR) [21]. The particle phase signals were integrated over the thermal desorption cycles and are reported in ion counts. Post-processing analysis was carried out in Python using the packages Matplotlib and Pandas and in Openair which was used to generate polar plots (Figure S12)[22]. Use of ion counts rather than calibrated signal when comparing data from different ions comes with uncertainties due to the enhanced sensitivity of iodide as a reagent ion to oxygenated organic compounds [23]. This can result in an overestimation of the importance of more oxidised compounds relative to less oxidised ones. This difference in relative detection sensitivities of the I^- reagent ion does not affect the mass spectra or the time series of the factors extracted from the PMF analysis performed in this study. Since the mass concentrations attributed to each factor is affected by the I^- detection sensitivity, for comparison with AMS measurements, a calibration factor based on that of levoglucosan [24] was applied to the summed particle phase signal of ions detected by CIMS. Levoglucosan was chosen as a calibrant for this comparison as iodide has near collision limit sensitivity to this species [25].

Peak identification was carried out for the particle phase mass spectra, with a peak list developed based upon study of laboratory oxidation of aromatics [26]. The peak lists derived from this study were combined and applied to several spectra from the field campaign, the fits were checked and additional ions were fitted where there was a residual, typically those with biogenic sources. A filtering criteria, described in detail in the supplement, was applied to select 177 ions for the PMF analysis. Various studies show that aerosols can undergo thermal decomposition within the FIGAERO inlet [27–29] While these ions themselves cannot be used as ambient markers for chemistry, many are included in this study as their temporal trends can act as a proxy for their parent ions as these have proven useful in previous studies in establishing source contributions [30]. Due to many isomers of a given ion being potentially observed in ambient measurements, unambiguously determining the contribution of ions which are produced from thermal decomposition is challenging. It should thus be noted that many such ions are included in calculation of bulk factor properties which may be more oxidised than the real aerosol components they represent.

The ambient spectrum was fitted with over 1500 peaks, of which 396 were identified and assigned. Of the identified ions, there were 355 ions which contain carbon, hydrogen and oxygen only (CHO) and 41 which contain carbon, hydrogen, oxygen and nitrogen (CHON). These can be seen in Figure S2, though it should be noted that abundant ions have been removed for readability ($C_3H_6O_3$, CH_2O_2, CH_4N_2O, $C_8H_4O_4$, $C_4H_2O_4$ and $C_4H_2NO_2$). Due to use of an x-ray ionisation source in this study, reagent ion availability is much lower than that in studies which utilise Po-210. As a result, many ions are observed at poor signal-to-noise ratios. In order to filter the identified ions, their thermal desorption profiles were inspected and those which exhibited noisy time series with no clear thermal desorption from the filter, were not included in further analysis (Figure S2). Thus the selection of ions utilised for analysis herein consists of 177 ions sub-selected from the 396 ions which were identified and assigned, of which 165 are CHO and 12 are CHON, contributing 75 and 25 % of signal, respectively. It should be noted that this method of selection of ions has the potential to introduce bias into the characterisation of SOA given that our sum formulas do not include contributions from other species which we were unable to identify. If these species could be identified, they could highlight very different chemical signatures.

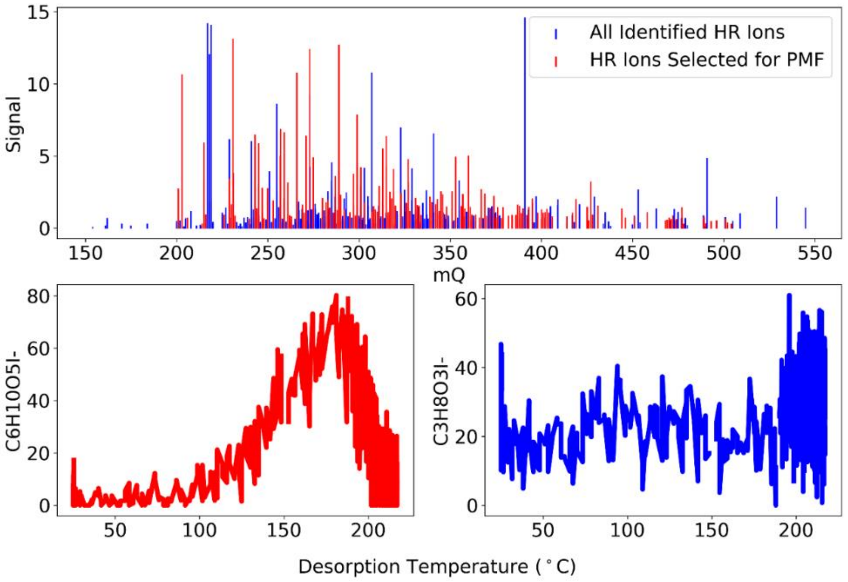

Figure S2 Average aerosol phase mass spectrum of ions identified during the measurement campaign (top) with examples of typical thermal desorption profiles of the ions selected for PMF and those identified but not included in the PMF

1.4. Positive Matrix Factorisation

Positive matrix factorisation (PMF) is an approach commonly used for source apportionment of online AMS measurements [31–33] and has more recently been applied to CIMS measurements to evaluate the sources and chemistry of ambient trace gases and aerosols [30,34–37].

The PMF algorithm deconvolves observed data as a linear combination of factors, each of which has a constant mass spectral profile and varying temporal contributions across a measurement period. Of the wide range of dimensionality reduction techniques available, it is particularly suited for use with mass spectral datasets as it is able to apportion a single ion to multiple factors [38]. This is particularly important for interpretation of CIMS factors, where a single ion can represent various isomers from different sources and oxidation pathways. In addition, it only allows positive factors, which is important for mass spectrometers as an ion counting technique which cannot give negative results. For application of PMF to FIGAERO-CIMS data, each thermogram was first integrated (233 desorption cycles) and the errors estimated using Poisson statistics:

$$\sigma = \sqrt[2]{I}$$

Where I is the integrated ion signal in counts. However, as highlighted by Chen et al. (2020), this provides an underestimation of the noise. Additional sources of noise in FIGAERO-CIMS ion measurements can arise from the thermal desorption process, which varies across the desorption profile. Thus, we apply the same approach used by Chen et al. (2020) in which a noise scaling factor is empirically derived based on the variability between pairs of highly correlated ions. In this study a scaling factor of 5 is found to be sufficient to describe the variability. The relationship between highly correlated ions are shown in Figure S3, where the left panel has error bars on each point of the unscaled noise, and the right, of the scaled noise. This figure shows that the scaled noise encompasses the variability of these highly correlated ions, and thus represents a truer estimate of the uncertainty than that of the unscaled noise.

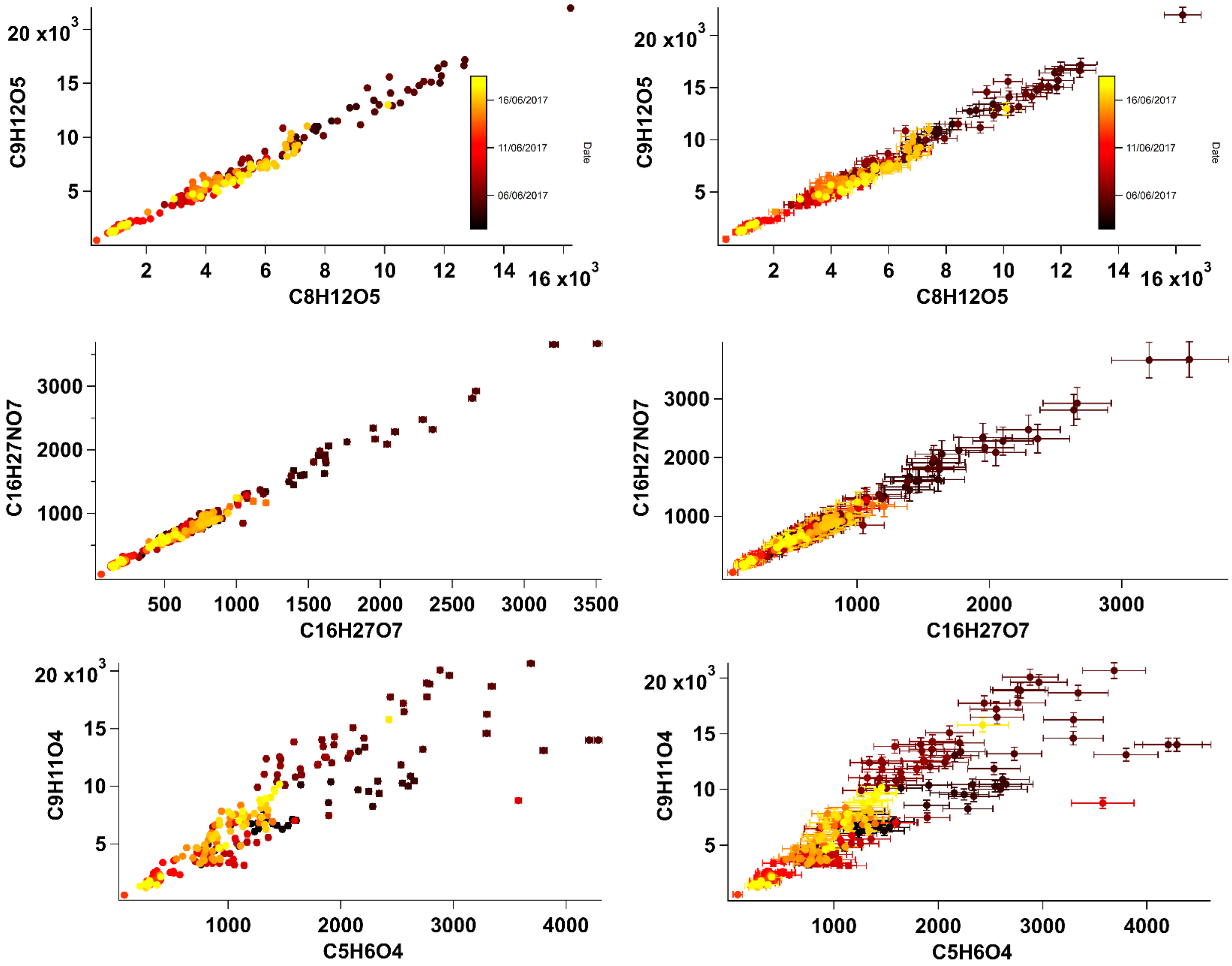

Figure S3 - Scatter plots of ion signal of highly-correlated ions with error bars showing estimated errors by Poisson statistics (left) and after scaling by a factor of 5 (right).

The PMF algorithm was implemented within the Igor Pro based PMF evaluation tool (v. 3.01) [6] and PMF runs with up to 10 factors were examined. As described in previous publications[2–4,6] , the choice of solution can be ambiguous and here we select the 'best' solution based on mathematical diagnostics as well as interpretability of solutions. These diagnostics typically include the Q-value, which is the total sum of the squares of the scaled residuals. This is evaluated against the expected error, and if all points in the matrix are fitted within their expected error then the expected Q (Q_{exp}) equals the degrees of freedom of the fitted data[7]. An optimum solution is defined as one where the modelled Q value approaches the expected Q values, yielding a Q/Q_{exp} *of* ~ 1.

The mathematical diagnostics included investigation of the decrease in total Q/Q_{exp} with increase in factor number (Figure S6) as well as the distribution of Q with time (Figure S4) and m/z (Figure S5). The PMF solution that explains the most variability whilst also being interpretable is chosen as the "best" solution. The interpretability of the solutions is investigated by identification and separation of mass spectral ions that are known to be fingerprints of distinct sources as well as temporal correlation with changes in meteorological conditions and/or other ancillary tracers of sources of atmospheric ageing process. Taking all these factors together, the result of a single PMF analysis which was run for the entire dataset was a final factor solution of 8 factors with a Q/Q_{exp} of close to 1.

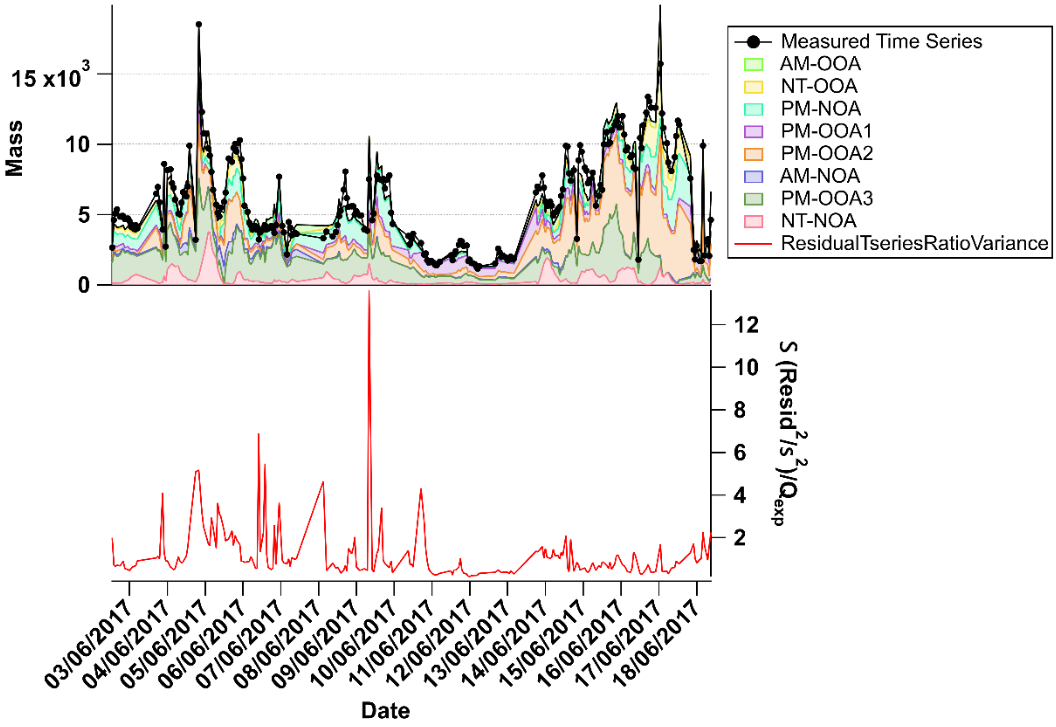

Figure S4 – Time Series of Stacked Factors compared with measured time series (top) and squared scaled residuals for each time point (bottom)

The algorithm reconstructs the data matrix by the linear combination of factors, and Figure S4 (top) shows a comparison of the reconstructed time series of the total signal split by factors with that of the measured time series (black). This shows that the reconstructed time series agrees with that measured, except in the case of a point on 09/06/2017 08:00, where the model overestimates observed signal. This is further reflected in the squared scaled residuals for each point in time, shown in Figure S4 (bottom), which shows a sharp spike at the same time point. It is likely that this spike corresponds to poorly characterised mixing down from the residual layer, the magnitude of which the PMF model is unable to capture or a vehicle related emission plume, given that the spike is most well represented by AM-OOA, which is abundant during this time. As can be seen in the total Q/Q_{exp} with number of factors, additional factors do not significantly reduce the Q/Q_{exp} or better explain distinct events in Q/Q_{exp} in time or m/z dimensions and thus the 8 factor solution is chosen.

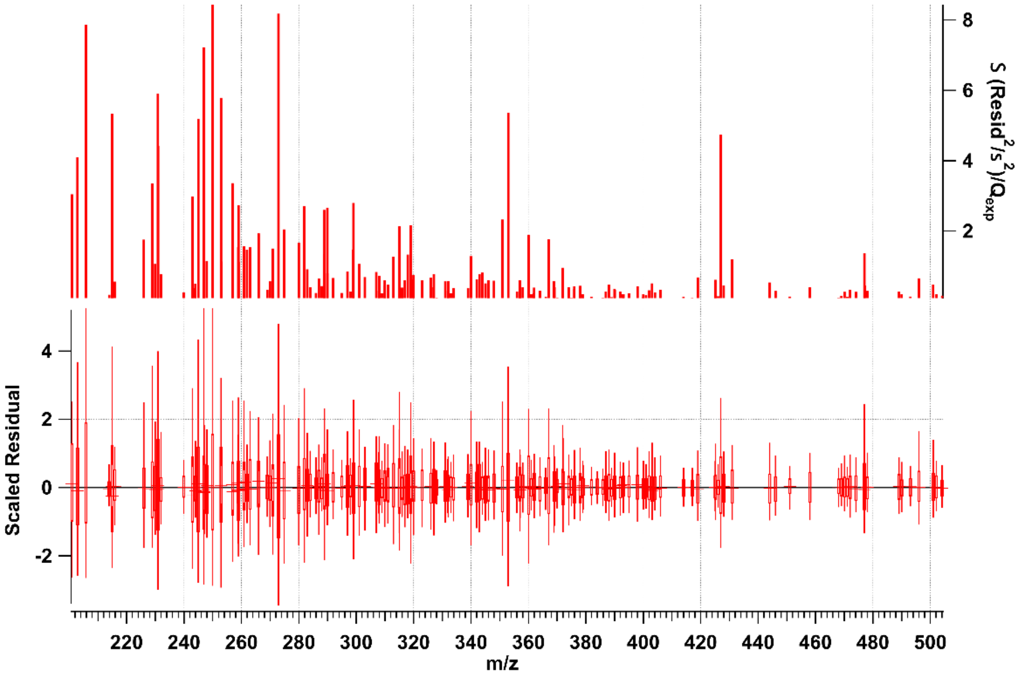

Figure S5 – Contribution of specific ions to the scaled residual.

While Figure S4 represents the temporal variability in the residual of the PMF, Figure S5 shows the key ions which contribute most to the residual. Figure S5 shows the total Q contribution as a function of m/z, and shows that some ions have a particularly high Q contribution, which include $C_5H_6O_5$, $C_2H_4O_3$ and $C_4H_8O_4$, with the remainder showing a relatively similar contribution. Box and whisker plots of the scaled residuals of each species are shown in Figure Y. The 8 factor solution is selected as optimum as the scaled residuals do not show any ions which have distinctly higher residuals from one another. Finally, the Q/Q_{exp}variability with number of factors (Figure S6) shows the quality of the fit of model to observations, and the 8 factor solution is at the asymptote of this curve, fewer factors significantly reduce the amount of measured variability that can be described by the PMF, while more factors are unable to capture significantly more. Thus, this alongside the interpretability of the solutions is why eight factor is selected as the optimum solution.

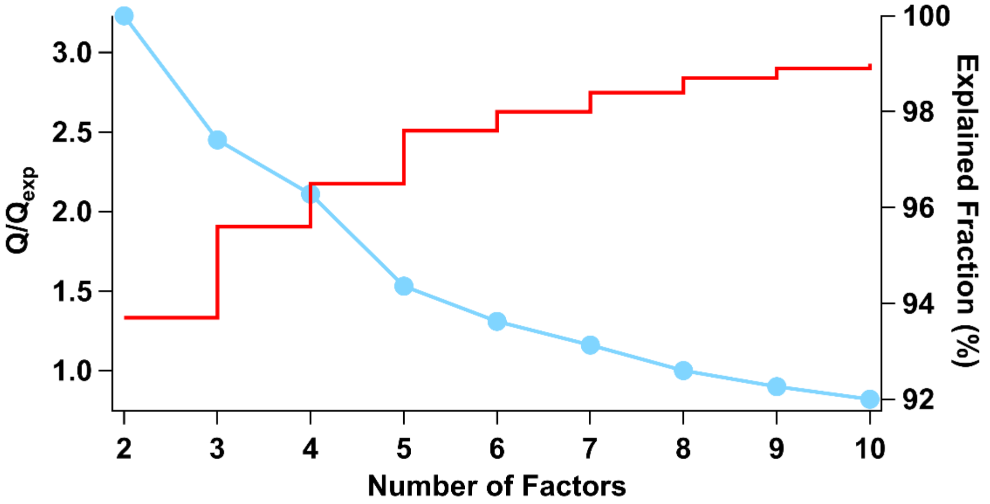

Figure S6 – Q/Q_{exp} and explained fractional variation over number of factors

2. Time Periods & Aerosol Composition

Parameter	Period 1	Period 2	Period 3
Average daytime O_3 (ppb)	58	57	93
Average daytime OH (molecules cm^{-3})	4.4×10^6	6.7×10^6	7.7×10^6
Average night time NO_3 (ppt)	3	8	16
Average NO_x (ppb)	26	39	21
Average wind speed ($m\ s^{-1}$)	2	2	2
Average Temperature (°C)	23	26	31
Average RH (%)	45	32	31

Table S1 – Criteria used for defining different time periods over the measurement period.

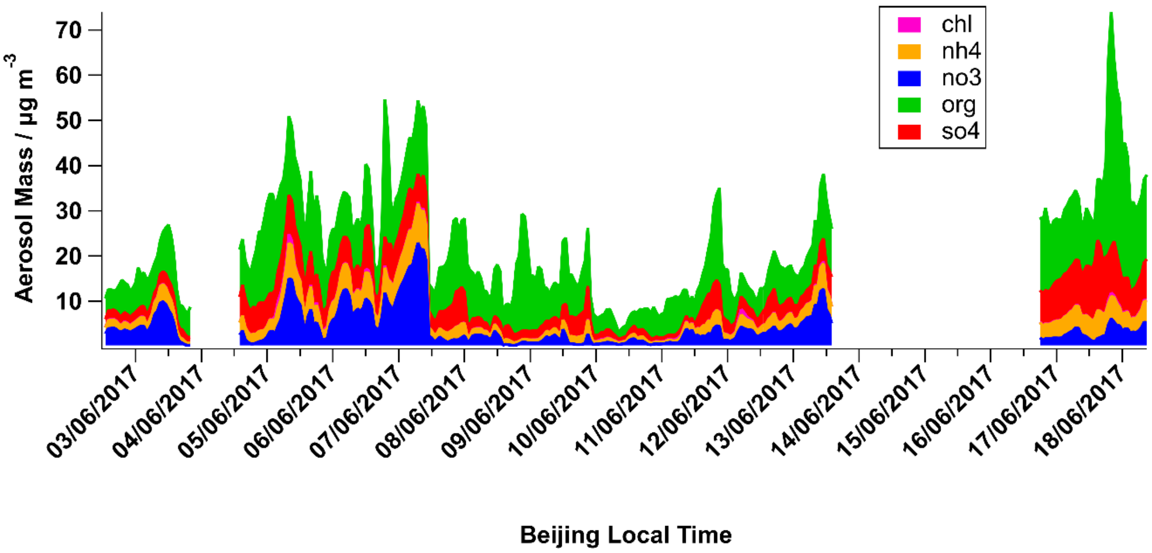

Figure S7 – Time series of PM_1 aerosol components as measured by the AMS

Parameter	Period 1	Period 2	Period 3
Average PM_1 ($\mu g\ m^{-3}$)	27	15	37
Organics (%)	41	54	54
Sulphate (%)	19	18	27
Nitrate (%)	26	16	8
Chloride (%)	1	1	1
Ammonium (%)	13	11	10

Table S2 – Contribution of different aerosol components to PM_1 during different time periods

3. Factor Mass Spectra and Composition Tables

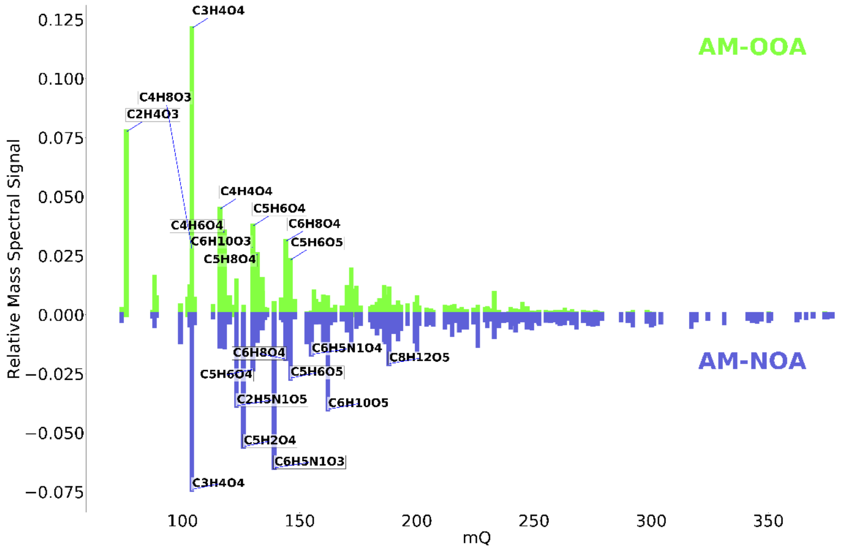

Figure S8 Mass Spectra of Morning Factors (AM-OOA and AM-NOA)

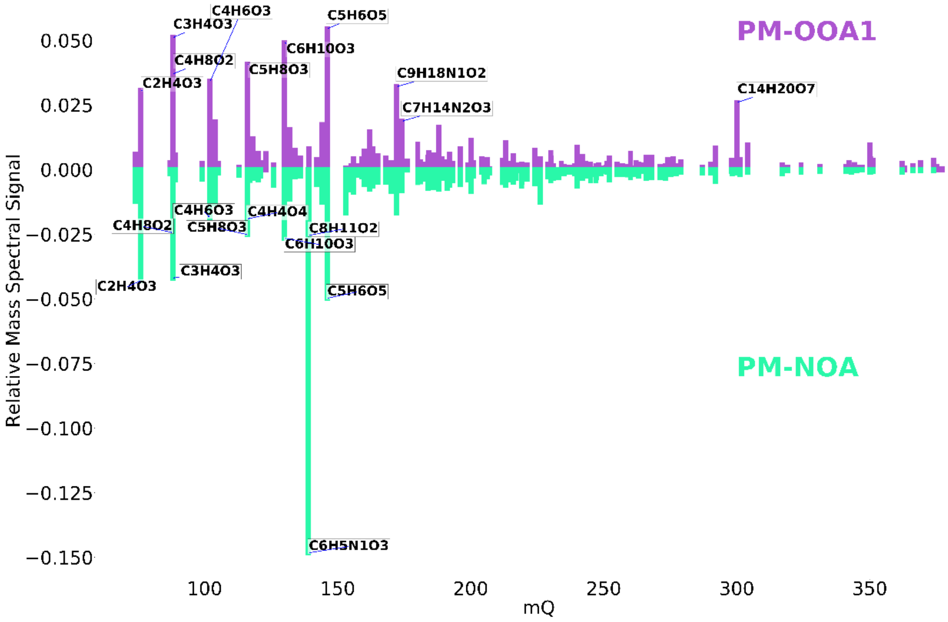

Figure S9 High-NOx Afternoon Factors (PM-OOA1 and PM-NOA)

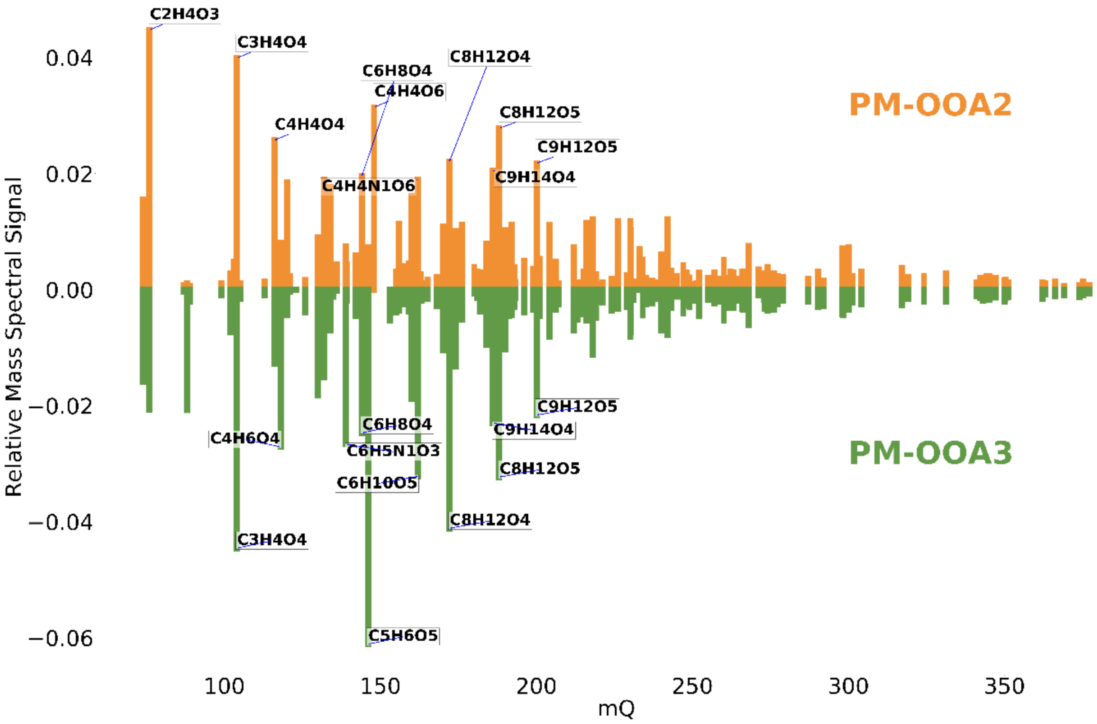

Figure S10 Low-NOx Afternoon Factors (PM-OOA2 and PM-OOA3)

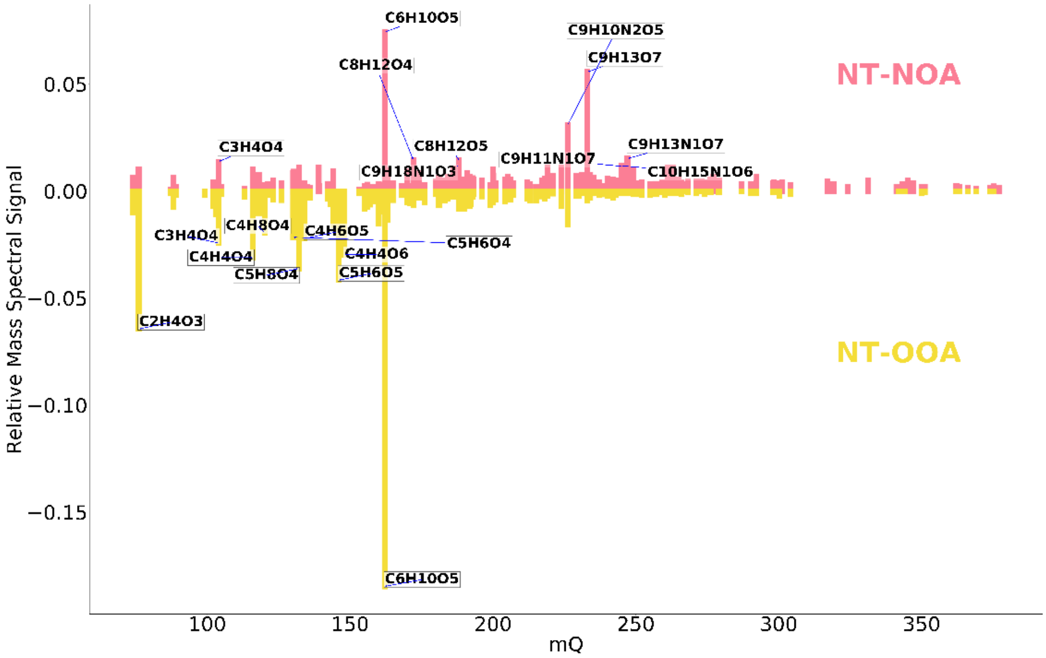

Figure S11 Night-time Factor Mass Spectra (NT-NOA and NT-OOA)

sumFormula	AM-OOA_%	Observed from Aromatics	No. of factors with ion in Top 20
C3H4O4	12.1	TRUE	6
C2H4O3	7.7	TRUE	6
C4H4O4	4.5	TRUE	6
C5H6O4	3.8	TRUE	4
C4H6O4	3.5	TRUE	5
C6H8O4	3.1	TRUE	5
C6H10O3	2.8	TRUE	5
C4H8O3	2.8	TRUE	4
C5H8O4	2.6	TRUE	6
C5H6O5	2.3	TRUE	6
C8H12O4	1.9	TRUE	7
C5H8O3	1.7	TRUE	4
C3H4O3	1.6	TRUE	4
C6H12N2O2	1.5	TRUE	3
C4H6O5	1.5	TRUE	3
C2H5N1O5	1.4	FALSE	2
C5H12N2O2	1.2	TRUE	3
C4H7O3	1.2	TRUE	2
C9H14O4	1.2	TRUE	5
C4H8O2	1.2	FALSE	3

Table S3 Top 20 ions by signal contribution to AM-OOA

sumFormula	NT-OOA_%	Observed from Aromatics	No. of factors with ion in Top 20
C6H10O5	18.5	TRUE	5
C2H4O3	6.4	TRUE	6
C5H6O5	4.2	TRUE	6
C5H8O4	3.6	TRUE	6
C4H4O4	3.1	TRUE	6
C4H4O6	3.0	TRUE	2
C3H4O4	2.4	TRUE	6
C4H6O5	2.2	TRUE	3
C5H6O4	2.2	TRUE	4
C4H8O4	2.0	TRUE	2
C6H8O4	1.6	TRUE	5
C9H10N2O5	1.6	TRUE	4
C6H8O5	1.5	TRUE	4
C4H4O5	1.4	TRUE	2
C6H10O3	1.4	TRUE	5
C6H11O5	1.4	TRUE	1
C5H8O3	1.2	TRUE	4
C5H10O4	1.2	TRUE	1

C4H7O3	1.1	TRUE	2
C4H6O4	1.0	TRUE	5

Table S4 Top 20 ions by signal contribution to NT-OOA

sumFormula	PM-NOA_%	Observed from Aromatics	No. of factors with ion in Top 20
C6H5N1O3	14.9	FALSE	4
C5H6O5	5.0	TRUE	6
C2H4O3	4.3	TRUE	6
C3H4O3	4.2	TRUE	4
C6H10O3	2.7	TRUE	5
C8H11O2	2.6	FALSE	1
C5H8O3	2.5	TRUE	4
C4H8O2	2.4	FALSE	3
C4H4O4	1.9	TRUE	6
C4H6O3	1.9	TRUE	2
C7H7N1O3	1.7	FALSE	2
C9H18N1O2	1.7	FALSE	3
C4H8O3	1.3	TRUE	4
C8H12O4	1.3	TRUE	7
C6H12N2O2	1.3	TRUE	3
C9H10N2O5	1.3	TRUE	4
C2H2O3	1.2	TRUE	3
C5H8O4	1.1	TRUE	6
C5H12N2O2	1.1	TRUE	3
C6H4O5	0.9	TRUE	1

Table S5 Top 20 ions by signal contribution to PM-NOA

sumFormula	PM-OOA1_%	Observed from Aromatics	No. of factors with ion in Top 20
C5H6O5	5.5	TRUE	6
C3H4O3	5.1	TRUE	4
C6H10O3	4.9	TRUE	5
C5H8O3	4.1	TRUE	4
C4H8O2	3.7	FALSE	3
C4H6O3	3.4	TRUE	2
C9H18N1O2	3.2	FALSE	3
C2H4O3	3.1	TRUE	6
C14H20O7	2.6	FALSE	1
C7H14N2O3	1.9	TRUE	2
C4H4O4	1.9	TRUE	6
C4H8O3	1.8	TRUE	4
C6H12N2O2	1.7	TRUE	3
C9H18N1O3	1.6	FALSE	3
C5H12N2O2	1.5	TRUE	3
C6H10O5	1.5	TRUE	5
C8H12O4	1.4	TRUE	7

C4H6O4	1.2	TRUE	5
C11H20O3	1.1	FALSE	1
C5H11N1O8	1.0	FALSE	1

Table S6 Top 20 ions by signal contribution to PM-OOA1

sumFormula	PM-OOA2_%	Observed from Aromatics	No. of factors with ion in Top 20
C2H4O3	4.5	TRUE	6
C3H4O4	4.0	TRUE	6
C4H4O6	3.2	TRUE	2
C8H12O5	2.8	TRUE	4
C4H4O4	2.6	TRUE	6
C8H12O4	2.2	TRUE	7
C9H12O5	2.2	TRUE	4
C9H14O4	2.1	TRUE	5
C6H8O4	2.0	TRUE	5
C4H4N1O6	1.9	FALSE	1
C5H8O4	1.9	TRUE	6
C4H8O4	1.9	TRUE	2
C4H6O5	1.8	TRUE	3
C4H4O5	1.8	TRUE	2
C6H8O5	1.6	TRUE	4
C4H8O3	1.6	TRUE	4
C2H2O3	1.6	TRUE	3
C3H4O5	1.3	TRUE	1
C12H18O5	1.2	FALSE	1
C9H14O6	1.2	TRUE	1

Table S7 Top 20 ions by signal contribution to PM-OOA2

sumFormula	AM-NOA_%	Observed from Aromatics	No. of factors with ion in Top 20
C3H4O4	7.4	TRUE	6
C6H5N1O3	6.5	FALSE	4
C5H2O4	5.6	TRUE	1
C6H10O5	4.0	TRUE	5
C2H5N1O5	3.9	FALSE	2
C5H6O5	2.7	TRUE	6
C5H6O4	2.3	TRUE	4
C8H12O5	2.1	TRUE	4
C6H8O4	1.9	TRUE	5
C6H5N1O4	1.7	FALSE	1
C9H12O5	1.5	TRUE	4
C4H6O4	1.4	TRUE	5
C4H4O4	1.4	TRUE	6
C8H12O4	1.3	TRUE	7
C9H10N2O5	1.3	TRUE	4
C9H14O4	1.2	TRUE	5
C6H11O1	1.2	FALSE	1

C6H8O5	1.2	TRUE	4
C7H7N1O3	1.1	FALSE	2
C9H11O5	1.1	TRUE	1

Table S8 Top 20 ions by signal contribution to AM-NOA

sumFormula	PM-OOA3_%	Observed from Aromatics	No. of factors with ion in Top 20
C5H6O5	6.1	TRUE	6
C3H4O4	4.5	TRUE	6
C8H12O4	4.1	TRUE	7
C8H12O5	3.2	TRUE	4
C6H10O5	3.2	TRUE	5
C4H6O4	2.7	TRUE	5
C6H5N1O3	2.7	FALSE	4
C6H8O4	2.5	TRUE	5
C9H14O4	2.3	TRUE	5
C9H12O5	2.2	TRUE	4
C3H4O3	2.1	TRUE	4
C2H4O3	2.1	TRUE	6
C6H8O5	1.9	TRUE	4
C9H18N1O2	1.8	FALSE	3
C5H6O4	1.8	TRUE	4
C6H10O3	1.7	TRUE	5
C2H2O3	1.6	TRUE	3
C5H8O4	1.5	TRUE	6
C9H18N1O3	1.4	FALSE	3
C7H14N2O3	1.3	TRUE	2

Table S9 Top 20 ions by signal contribution to PM-OOA3

sumFormula	NT-NOA_%	Observed from Aromatics	No. of factors with ion in Top 20
C6H10O5	7.4	TRUE	5
C9H13O7	5.6	TRUE	1
C9H10N2O5	3.1	TRUE	4
C9H13N1O7	1.5	FALSE	1
C8H12O4	1.5	TRUE	7
C8H12O5	1.4	TRUE	4
C3H4O4	1.4	TRUE	6
C9H18N1O3	1.2	FALSE	3
C10H15N1O6	1.2	FALSE	1
C9H11N1O7	1.2	FALSE	1
C12H11O4	1.1	FALSE	1
C11H19O7	1.1	FALSE	1
C14H13O5	1.1	FALSE	1
C5H8O4	1.1	TRUE	6
C6H5N1O3	1.1	FALSE	4
C10H8O6	1.1	TRUE	1

C9H14O4	1.1	TRUE	5
C9H13N1O8	1.1	FALSE	1
C9H12O5	1.0	TRUE	4
C9H15N1O7	1.0	FALSE	1

Table S10 Top 20 ions by signal contribution to NT-NOA

sumFormula	AM-OOA_perc	AM-OOA_R	Observed by Mehra et al. (2020)	Identification/ Other Source(s)	Reference
C4H4O4	4.5	0.73	TRUE	α- pinene	39
C4H7O3	1.2	0.72	TRUE	-	-
C3H4O4	12.1	0.71	TRUE	Malonic Acid / 3-oxoperoxypropanoic acid (α- pinene)	40
C4H8O3	2.8	0.70	TRUE	Isoprene dihydroxy carbonyl	41
C5H9O3	0.9	0.69	TRUE	-	-
C2H4O3	7.7	0.69	TRUE	Glycolic acid	42
C4H5O4	0.8	0.68	TRUE	Naphthalene Oxidation Product	43
C3H5O4	0.7	0.68	TRUE	-	-
C4H6O5	1.5	0.66	TRUE	Guaiacol Oxidation Product / Phenol Oxidation Product	44,45
C5H6O4	3.8	0.66	TRUE	Guaicol Oxidation Product / Isoprene Oxidation Product / Lignite Combustion	44,46,47
C3H5O3	0.7	0.65	TRUE	-	-
C5H10O4	0.9	0.65	TRUE	Isoprene Oxidation Product	48,49
C5H5O3	0.3	0.65	TRUE	1,3,5-Trimethyl benzene	50
C6H4O5	1.0	0.64	TRUE	-	-
C7H9O4	0.6	0.63	TRUE	Terebic acid (α-pinene)	51
C5H12N2O2	1.2	0.62	TRUE	Aqueous Methylglyoxal Oxidation product	52
C6H12N2O2	1.5	0.62	TRUE	Aqueous Methylglyoxal Oxidation product	52
C4H4O5	1.1	0.62	TRUE	α- pinene / aged toluene SOA	39,53
C6H7O4	0.4	0.61	TRUE	Ambient	54
C7H7O5	0.4	0.59	TRUE	Vehicle Emissions	55

Table S11 Top 20 ions by Correlation with Factor Time Series for AM-OOA

sumFormula	NT-OOA_perc	NT-OOA_R	Observed from Aromatics	Other Source(s)	Reference
C4H4O6	3.0	0.79	TRUE	Tartaric Acid	[56]
C4H4N1O6	1.0	0.69	FALSE	-	-
C4H6O5	2.2	0.69	TRUE	Guaiacol Oxidation Product / Phenol Oxidation Product	[44,45]
C3H4O5	1.0	0.69	TRUE	Maleic Acid Aerosol, Aqueous Processing	[57,58]
C5H10O4	1.2	0.67	TRUE	Isoprene Oxidation Product	[48,49]
C4H4O5	1.4	0.67	TRUE	α- pinene / aged toluene SOA	[39,53]
C5H12O3	0.7	0.67	TRUE	IEPOX + ISOPOOH	[59]
C6H10O5	18.5	0.64	TRUE	Levoglucosan, α-pinene	[60,61]
C2H4O3	6.4	0.63	TRUE	Glycolic acid	[42]
C7H7O5	0.6	0.62	TRUE	Vehicle Emissions	[55]
C6H7O4	0.6	0.61	TRUE	Ambient	[54]
C6H4O5	0.8	0.60	TRUE	-	-
C5H8O4	3.6	0.59	TRUE	Glutaric Acid, methylsuccinic acid, Isoprene oxidation product	[62–64]
C5H12N2O2	0.8	0.57	TRUE	Aqueous Methylglyoxal Oxidation product	[52]
C4H8O4	2.0	0.57	TRUE	2-methylglyceric acid	[65]
C7H9O4	0.6	0.56	TRUE	Terebic acid (α-pinene)	[51]
C4H4O4	3.1	0.56	TRUE	α- pinene	[39]
C6H12N2O4	0.5	0.56	TRUE	Lignite combustion	[47]
C4H7O3	1.1	0.56	TRUE	-	-
C9H12O1	0.3	0.55	FALSE	Trimethylphenol	

Table S1 Top 20 ions by Correlation with Factor Time Series for NT-OOA

sumFormula	PM-NOA_perc	PM-NOA_R	Observed from Aromatics	Potential Source(s)	Reference
C8H11O2	2.6	0.76	FALSE	Ambient China	66
C6H5N1O3	14.9	0.66	FALSE	Nitrophenol	67,68
C4H5N1O6	0.3	0.54	FALSE	Nitrosuccinic acid	
C7H7N1O3	1.7	0.52	FALSE	Methyl nitrophenol	68
C4H4N1O6	0.7	0.52	FALSE	-	-
C5H12N2O2	1.1	0.50	TRUE	Aqueous Methylglyoxal Oxidation product	52

Table S2 Top 20 ions by Correlation with Factor Time Series for PM-NOA

sumFormula	PM-OOA2_perc	PM-OOA2_R	Observed from Aromatics	Other Source(s)	Reference
C4H4N1O6	1.9	0.795027	FALSE	-	-
C4H4O6	3.2	0.760491	TRUE	Tartaric Acid	56
C5H12O3	1.0	0.700304	TRUE	IEPOX + ISOPOOH	59
C4H4O5	1.8	0.671819	TRUE	α- pinene / aged toluene SOA	39,53
C8H8O7	1.1	0.671493	TRUE	1,3,5-trimethyl benzene, biomass burning	36,69
C3H4O5	1.3	0.66	TRUE	Maleic Acid Aerosol, Aqueous Processing	57,58
C9H12O1	0.4	0.66	FALSE	Trimethylphenol	
C6H12N2O4	1.1	0.63	TRUE	Lignite combustion	47
C6H4O5	1.1	0.59	TRUE	-	-
C9H10O7	1.2	0.57	TRUE	1,2,4-trimethyl benzene	70
C5H10O4	0.9	0.56	TRUE	Isoprene Oxidation Product	48,49
C13H26O3	0.5	0.55	FALSE	Cigarette Smoke	36
C4H6O5	1.8	0.55	TRUE	Guaiacol Oxidation Product / Phenol Oxidation Product	44,45
C2H4O3	4.5	0.55	TRUE	Glycolic acid	42

C5H12N2O2	0.9	0.54	TRUE	Aqueous methylglyoxal oxidation	[52]
C9H16O5	1.1	0.53	TRUE	1,3,5-trimethyl benzene	[71]
C4H8O4	1.9	0.52	TRUE	2-methylglyceric acid	[65]

Table S3 Top 20 ions by Correlation with Factor Time Series for PM-OOA2

sumFormula	AM-NOA_perc	AM-NOA_R	Observed from Aromatics (Mehra et al. 2020)	Other Source(s)	Reference
C5H2O4	5.6	0.97	TRUE	-	-
C6H11O1	1.2	0.91	FALSE	Cyclohexanol, 2-methyltetrahydropyran	-
C2H5N1O5	3.9	0.91	FALSE	-	-
C6H5N1O4	1.7	0.82	FALSE	4-nitrocatechol	[72]
C3H4O4	7.4	0.80	TRUE	Malonic Acid / 3-oxoperoxypropanoic acid (α- pinene)	[40]
C9H11O5	1.1	0.78	TRUE	Syringic Acid from Biomass burning	[73]
C9H11O6	0.9	0.75	TRUE	-	-
C7H5N1O5	0.8	0.75	FALSE	Perbenzoyl Nitrate (Biomass Burning – Oxidation of Benzaldehyde)	[74]
C3H5O4	0.4	0.74	TRUE	-	-
C5H6O4	2.3	0.73	TRUE	Guaicol Oxidation Product / Isoprene Oxidation Product / Lignite Combustion	[44,46,47]
C4H5O4	0.4	0.70	TRUE	Naphthalene Oxidation Product	[43]
C6H6O3	0.5	0.69	TRUE	Phenol oxidation product	[44]
C7H7N1O3	1.1	0.67	FALSE	Methyl Nitrophenol	[68]
C5H9O3	0.4	0.66	TRUE	-	-
C11H13O3	0.5	0.65	FALSE	-	-
C6H8O4	1.9	0.63	TRUE	Phenol Oxidation product	(Yee et al., 2013)
C9H11O4	0.5	0.63	TRUE	Ambient China	[66]
C9H4O5	1.0	0.62	TRUE	-	-
C4H6O4	1.4	0.62	TRUE	Emissions from Buses	[55]
C6H9N1O7	0.4	0.61	FALSE	1,3,5-trimethyl benzene (High NOx), Boreal Forest Measurements	[75,76]

Table S4 Top 20 ions by Correlation with Factor Time Series for AM-NOA

sumFormula	PM-OOA3_perc	PM-OOA3_R	Observed from Aromatics	Other Source(s)	Reference
C9H10O7	0.8	0.72	TRUE	1,2,4-trimethyl benzene SOA	70
C2H2O3	1.6	0.72	TRUE	glyoxylic acid, guacicol ring fragment	44,77
C10H12O8	0.5	0.70	TRUE	Pinnae diol new particle formation	78
C9H12N3O7	0.4	0.69	TRUE	-	-
C8H8O7	0.5	0.69	TRUE	1,3,5-trimethyl benzene, biomass burning	36,69
C9H14O6	1.1	0.69	TRUE	MBCTA from terpene oxidation	79
C8H12O4	4.1	0.68	TRUE	Pinene oxidation	80
C10H16N1O5	0.7	0.67	FALSE	-	-
C18H18O4	0.4	0.66	FALSE	Lignin Pyrolysis	81
C9H16O5	0.8	0.66	TRUE	1,3,5-trimethyl benzene, Wood burning	71,82
C13H26O3	0.3	0.65	FALSE	Cigarette Smoke	36
C10H10O7	0.7	0.6	FALSE	-	-
C5H6O5	6.1	0.64	TRUE	Toluene	53
C7H10O6	1.0	0.64	TRUE	Guaiacol Oxidation	44
C19H18O6	0.1	0.64	FALSE	Lignin Pyrolysis	36,83
C8H12O5	3.2	0.64	TRUE	Limonene SOA	84
C17H16O3	0.6	0.64	FALSE	-	-
C6H8O5	1.9	0.63	TRUE	Biomass Burning	44
C11H20O3	1.0	0.63	FALSE	Aqueous alpha-pinene SOA	85
C9H14O4	2.3	0.63	TRUE	Pinic acid	61

Table S5 Top 20 ions by Correlation with Factor Time Series for PM-OOA3

sumFormula	NT-NOA_perc	NT-NOA_R	Observed from Aromatics	Potential Source(s)	References
C9H13O7	5.6	0.92	TRUE	-	-
C10H15N1O6	1.2	0.88	FALSE	Terpene Nitrate	37,86
C11H19O7	1.1	0.88	FALSE	-	-
C9H11N1O7	1.2	0.86	FALSE	1,2,4-trimethyl benzene Oxidation Product	70

C9H13N1O8	1.1	0.86	FALSE	Terpene Nitrate and 1,2,4-trimethyl benzene oxidation product	70,86
C10H19N1O7	0.5	0.85	FALSE	Terpene nitrate	86
C14H13O5	1.1	0.85	FALSE	-	-
C11H19O6	0.9	0.84	FALSE	α- pinene	77
C9H13N1O7	1.5	0.84	FALSE	Terpene Nitrate and high-NOx 1,3,5-trimethyl benzene	75,86
C10H17N1O5	0.8	0.83	FALSE	Beta-pinene nitrate	87
C15H25N1O9	0.2	0.82	FALSE	Beta-caryophyllene + NOx	88
C9H10N2O5	3.1	0.82	TRUE	-	-
C9H13N1O9	0.5	0.82	FALSE	Terpene nitrate	86
C15H25N1O8	0.4	0.81	FALSE	Beta-caryophyllene + NOx	88
C16H27N1O7	0.5	0.81	FALSE	Beta-caryophyllene + NOx	88
C9H15N1O7	1.0	0.81	FALSE	Terpene Nitrate	37,86
C16H25N1O9	0.2	0.81	FALSE	Aerosol Cloud Water	89
C21H29O6	0.1	0.80	FALSE	-	-
C12H21O7	0.7	0.80	FALSE	-	-
C10H15N1O5	0.7	0.80	FALSE	Terpene nitrate	86

Table S6 Top 20 ions by Correlation with Factor Time Series for NT-NOA

4. Interpretation of Factor Sources

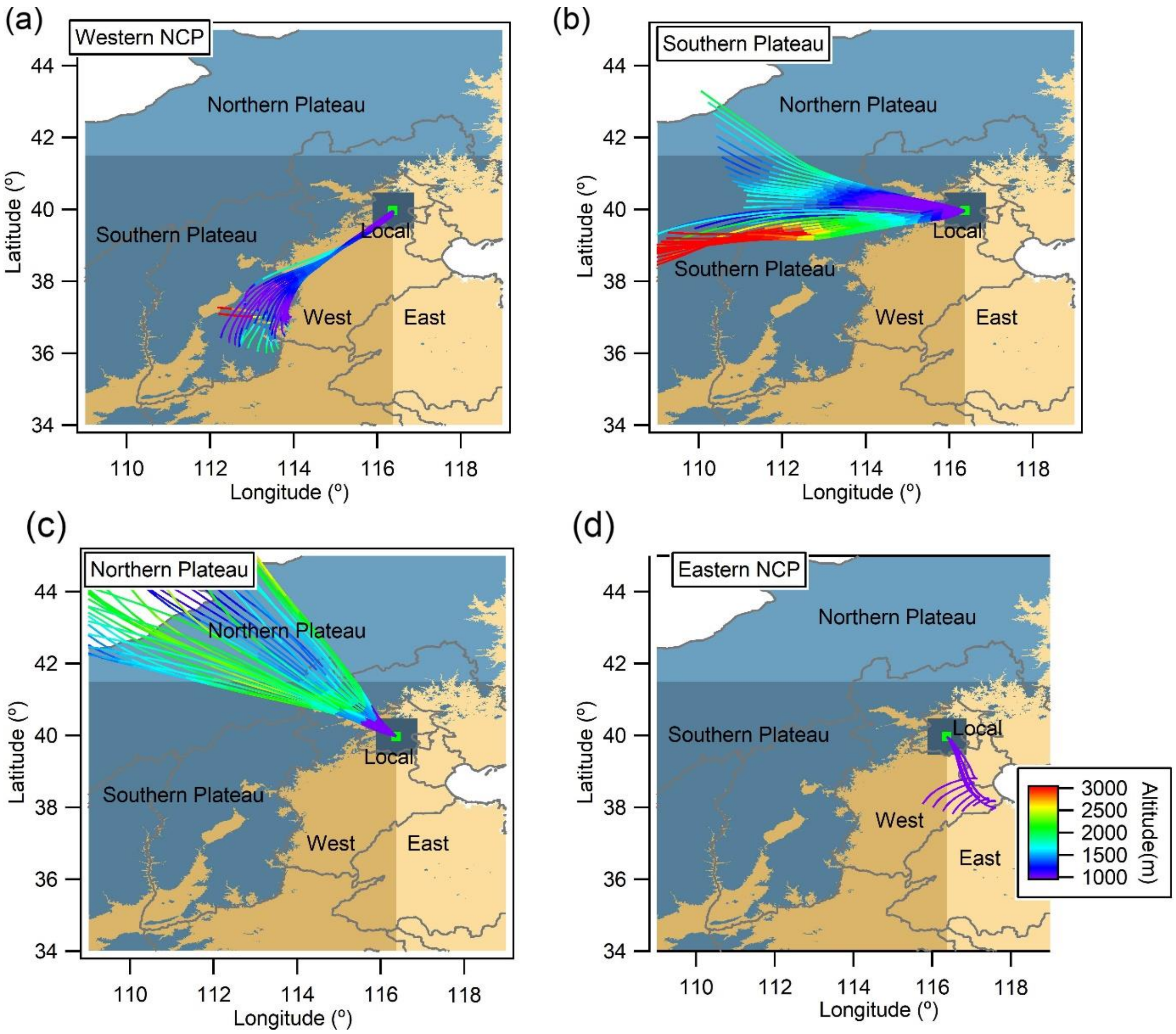

Figure S12 – Air mass origin classification map from Liu et al. (2019)

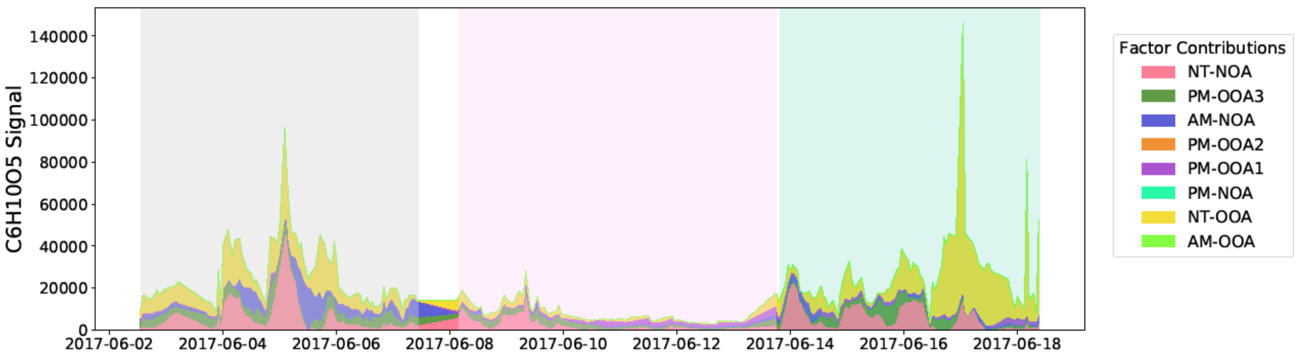

Figure S13 – Splitting of C6H10O5 ion between Factors

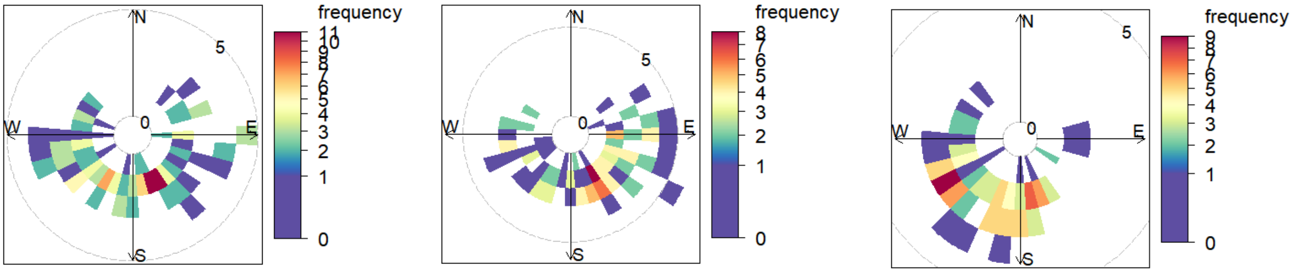

Period 1

Period 2

Period 3

Figure S14 – Wind Rose Plots for the three time periods

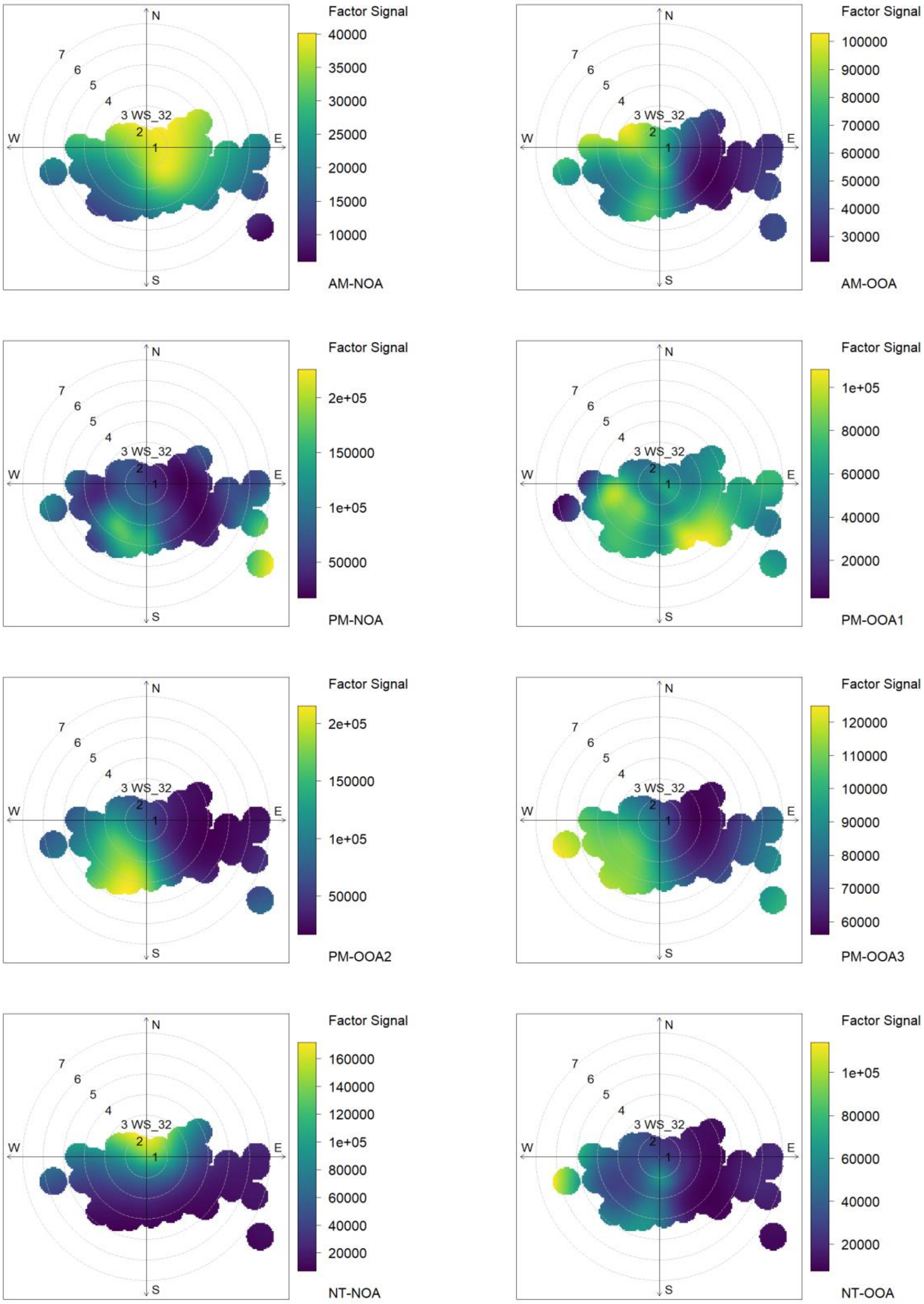

Figure S15 – Polar Plots from Openair for Factor Time Series showing the ion signal as a function of wind direction and speeds

References

1 F. D. Lopez-Hilfiker, C. Mohr, M. Ehn, F. Rubach, E. Kleist, J. Wildt, T. F. Mentel, A. Lutz, M. Hallquist, D. Worsnop and J. A. Thornton, *Atmos. Meas. Tech.*, 2014, **7**, 983–1001.

2 T. J. Bannan, M. Le Breton, M. Priestley, S. D. Worrall, A. Bacak, N. A. Marsden, A. Mehra, J. Hammes, M. Hallquist, M. R. Alfarra, U. K. Krieger, J. P. Reid, J. Jayne, W. Robinson, G. Mcfiggans, H. Coe, C. J. Percival and D. Topping, *Atmos. Meas. Tech*, 2019, **12**, 1429–1439.

3 E. J. Slater, L. K. Whalley, R. Woodward-Massey, C. Ye, J. D. Lee, F. Squires, J. R. Hopkins, R. E. Dunmore, M. Shaw, J. F. Hamilton, A. C. Lewis, L. R. Crilley, L. Kramer, W. Bloss, T. Vu, Y. Sun, W. Xu, S. Yue, L. Ren, W. Joe, F. Acton, C. N. Hewitt, X. Wang, P. Fu, D. E. Heard, D. Heard and L. Whalley, *Atmos. Chem. Phys. Discuss.*, , DOI:10.5194/acp-2020-362.

4 W. J. F. Acton, Z. Huang, B. Davison, W. S. Drysdale, P. Fu, M. Hollaway, B. Langford, J. Lee, Y. Liu, S. Metzger, N. Mullinger, E. Nemitz, C. E. Reeves, F. A. Squires, A. R. Vaughan, X. Wang, Z. Wang, O. Wild, Q. Zhang, Y. Zhang and ; C Nicholas Hewitt, *Atmos. Chem. Phys. Discuss.*, , DOI:10.5194/acp-2020-343.

5 L. K. Whalley, D. Stone, R. Dunmore, J. Hamilton, J. R. Hopkins, J. D. Lee, A. C. Lewis, P. Williams, J. Kleffmann, S. Laufs, R. Woodward-Massey and D. E. Heard, *Atmos. Chem. Phys.*, 2018, **18**, 2547–2571.

6 L. K. Whalley, M. A. Blitz, M. Desservettaz, P. W. Seakins and D. E. Heard, *Atmos. Meas. Tech.*, 2013, **6**, 3425–3440.

7 R. Woodward-Massey, E. J. Slater, J. Alen, T. Ingham, D. R. Cryer, L. M. Stimpson, C. Ye, P. W. Seakins, L. K. Whalley and D. E. Heard, *Atmos. Meas. Tech.*, 2020, **13**, 3119–3146.

8 R. Commane, C. F. A. Floquet, T. Ingham, D. Stone, M. J. Evans and D. E. Heard, *Atmos. Chem. Phys.*, 2010, **10**, 8783–8801.

9 O. J. Kennedy, B. Ouyang, J. M. Langridge, M. J. S. Daniels, S. Bauguitte, R. Freshwater, M. W. Mcleod, C. Ironmonger, J. Sendall, O. Norris, R. Nightingale, S. M. Ball and R. L. Jones, *Atmos. Meas. Tech*, 2011, **4**, 1759–1776.

10 W. P. Dube, S. S. Brown, H. D. Osthoff, M. R. Nunley, S. J. Ciciora, M. W. Paris, R. J. McLaughlin and A. R. Ravishankara, *Rev. Sci. Instrum.*, 2006, **77**, 034101.

11 W. Xu, Y. Sun, Q. Wang, J. Zhao, J. Wang, X. Ge, C. Xie, W. Zhou, W. Du, J. Li, P. Fu, Z. Wang, D. R. Worsnop and H. Coe, *J. Geophys. Res. Atmos.*, 2019, **124**, 1132–1147.

12 J. Brean, R. M. Harrison 1⍰, Z. Shi, D. C. S. Beddows, W. Joe, F. Acton and C. Nicholas Hewitt, , DOI:10.5194/acp-2019-156.

13 X.-F. Huang, L.-Y. He, M. Hu, M. R. Canagaratna, Y. Sun, Q. Zhang, T. Zhu, L. Xue, L.-W. Zeng, X.-G. Liu, Y.-H. Zhang, J. T. Jayne, N. L. Ng and D. R. Worsnop, *Atmos. Chem. Phys.*, 2010, **10**, 8933–8945.

14 J. Xu, Q. Zhang, M. Chen, X. Ge, J. Ren and D. Qin, *Atmos. Chem. Phys.*, 2014, **14**, 12593–12611.

15 C. Mohr, J. A. Huffman, M. J. Cubison and A. C. Aiken, *Environ. Sci. Technol.*, 2009, **43**, 2443–2449.

16 L.-Y. He, Y. Lin, X.-F. Huang, S. Guo, L. Xue, Q. Su, M. Hu, S.-J. Luan and Y.-H. Zhang, *Atmos. Chem. Phys.*, 2010, **10**, 11535–11543.

17 Y.-L. Sun, Q. Zhang, J. J. Schwab, K. L. Demerjian, W.-N. Chen, M.-S. Bae, H.-M. Hung, O. Hogrefe, B. Frank, O. V. Rattigan and Y.-C. Lin, *Atmos. Chem. Phys.*, 2011, **11**, 1581–1602.

18 S. C. Herndon, T. B. Onasch, E. C. Wood, J. H. Kroll, M. R. Canagaratna, J. T. Jayne, M. A. Zavala, W. B. Knighton, C. Mazzoleni, M. K. Dubey, I. M. Ulbrich, J. L. Jimenez, R. Seila, J. A. De Gouw, B. De Foy, J. Fast, L. T. Molina, C. E. Kolb and D. R. Worsnop, *Geophys. Res. Lett*, 2008, **35**, 15804.

19 J. R. Hopkins, C. E. Jones and A. C. Lewis, *J. Environ. Monit.*, 2011, 13, 2268–2276.

20 D. Bryant, W. Dixon, J. Hopkins, R. Dunmore, K. Pereira, M. Shaw, F. Squires, T. Bannan, A. Mehra, S. Worrall, A. Bacak, H. Coe, C. Percival, L. Whalley, D. Heard, E. Slater, B. Ouyang, T. Cui, J. Surratt, D. Liu, Z. Shi, R. Harrison, Y. Sun, W. Xu, A. Lewis, J. Lee, A. Rickard and J. Hamilton, *Atmos. Chem. Phys. Discuss.*, 2019, 1–30.

21 H. Stark, R. L. N. Yatavelli, S. L. Thompson, J. R. Kimmel, M. J. Cubison, P. S. Chhabra, M. R. Canagaratna, J. T. Jayne, D. R. Worsnop and J. L. Jimenez, *Int. J. Mass Spectrom.*, 2015, **389**, 26–38.

22 D. C. Carslaw and K. Ropkins, *Environ. Model. Softw.*, 2012, **27**–**28**, 52–61.

23 M. Riva, P. Rantala, J. E. Krechmer, O. Peräkylä, Y. Zhang, L. Heikkinen, O. Garmash, C. Yan, M. Kulmala, D. Worsnop and M. Ehn, *Atmos. Meas. Tech*, 2019, **12**, 2403–2421.

24 E. Reyes-Villegas, T. Bannan, M. Le Breton, A. Mehra, M. Priestley, C. Percival, H. Coe and J. D. Allan, *Environ. Sci. Technol.*, 2018, **52**, 5308–5318.

25 F. D. Lopez-Hilfiker, S. Iyer, C. Mohr, B. H. Lee, E. L. D'ambro, T. Kurtén and J. A. Thornton, *Atmos. Meas. Tech.*, 2016, **9**, 1505–1512.

26 A. Mehra, Y. Wang, J. E. Krechmer, A. Lambe, F. Majluf, M. A. Morris, M. Priestley, T. J. Bannan, D. J. Bryant, K. L. Pereira, J. F. Hamilton, A. R. Rickard, M. J. Newland, H. Stark, P. Croteau, J. T. Jayne, R. Worsnop, M. R. Canagaratna, L. Wang and H. Coe, *Atmos. Chem. Phys. Discuss*, , DOI:10.5194/acp-2020-161.

27 F. D. Lopez-Hilfiker, C. Mohr, E. L. D 'ambro, A. Lutz, T. P. Riedel, C. J. Gaston, S. Iyer, Z. Zhang, A. Gold, J. D. Surratt, B. H. Lee, T. Kurten, W. W. Hu, J. Jimenez, M. Hallquist and J. A. Thornton, *Environ. Sci. Technol.*, 2016, **50**, 2200–2209.

28 H. Stark, R. L. N. Yatavelli, S. L. Thompson, H. Kang, J. E. Krechmer, J. R. Kimmel, B. B. Palm, W. Hu, P. L. Hayes, D. A. Day, P. Campuzano-Jost, M. R. Canagaratna, J. T. Jayne, D. R. Worsnop and J. L. Jimenez, *Environ. Sci. Technol.*, 2017, **51**, 8491–8500.

29 S. Schobesberger, E. L. D'ambro, F. D. Lopez-Hilfiker, C. Mohr and J. A. Thornton, *Atmos. Chem. Phys*, 2018, **18**, 14757–14785.

30 Y. Chen, M. Takeuchi, T. Nah, L. Xu, M. R. Canagaratna, H. Stark, K. Baumann, F. Canonaco, A. S. H. Prévôt, L. G. Huey, R. J. Weber and N. L. Ng, *Atmos. Chem. Phys. Discuss*, , DOI:10.5194/acp-2020-126.

31 I. M. Ulbrich, M. R. Canagaratna, Q. Zhang, D. R. Worsnop and J. L. Jimenez, *Atmos. Chem. Phys.*, 2009, **9**, 2891–2918.

32 J. L. Jimenez, M. R. Canagaratna, N. M. Donahue, a. S. H. Prevot, Q. Zhang, J. H. Kroll, P. F. DeCarlo, J. D. Allan, H. Coe, N. L. Ng, a. C. Aiken, K. S. Docherty, I. M. Ulbrich, A. P. Grieshop, a. L. Robinson, J. Duplissy, J. D. Smith, K. R. Wilson, V. a. Lanz, C. Hueglin, Y. L. Sun, J. Tian, A. Laaksonen, T. Raatikainen, J. Rautiainen, P. Vaattovaara, M. Ehn, M. Kulmala, J. M. Tomlinson, D. R. Collins, M. J. Cubison, J. Dunlea, J. A. Huffman, T. B. Onasch, M. R. Alfarra, P. I. Williams,

K. Bower, Y. Kondo, J. Schneider, F. Drewnick, S. Borrmann, S. Weimer, K. Demerjian, D. Salcedo, L. Cottrell, R. Griffin, A. Takami, T. Miyoshi, S. Hatakeyama, A. Shimono, J. Y. Sun, Y. M. Zhang, K. Dzepina, J. R. Kimmel, D. Sueper, J. T. Jayne, S. C. Herndon, a. M. Trimborn, L. R. Williams, E. C. Wood, A. M. Middlebrook, C. E. Kolb, U. Baltensperger and D. R. Worsnop, *Science (80-.).*, 2009, **326**, 1525–1529.

33 Q. Zhang, J. L. Jimenez, M. R. Canagaratna, I. M. Ulbrich, N. L. Ng, D. R. Worsnop, Y. Sun, Q. Zhang, Y. Sun, J. L. Jimenez, I. M. Ulbrich, M. R. Canagaratna, N. L. Ng and D. R. Worsnop, *Anal. Bioanal. Chem.*, 2011, **401**, 3045–3067.

34 C. Yan, W. Nie, M. Äijälä, M. P. Rissanen, M. R. Canagaratna, P. Massoli, H. Junninen, T. Jokinen, N. Sarnela, S. Häme, S. Schobesberger, F. Canonaco, A. S. H. Prevot, T. Petäjä, M. Kulmala, M. Sipilä, D. R. Worsnop and M. Ehn, *Atmos. Chem. Phys.*, 2016, **16**, 12715–12731.

35 G. Stefenelli, V. Pospisilova, F. D. Lopez-Hilfiker, K. R. Daellenbach, C. Hüglin, Y. Tong, U. Baltensperger, A. S. H. Prévôt and J. G. Slowik, *Atmos. Chem. Phys*, 2019, **19**, 14825–14848.

36 L. Qi, M. Chen, G. Stefenelli, V. Pospisilova, Y. Tong, A. Bertrand, C. Hueglin, X. Ge, U. Baltensperger, A. S. H. Prévôt and J. G. Slowik, *Atmos. Chem. Phys.*, 2019, **19**, 8037–8062.

37 P. Massoli, H. Stark, M. R. Canagaratna, J. E. Krechmer, L. Xu, N. L. Ng, R. L. Mauldin, C. Yan, J. Kimmel, P. K. Misztal, J. L. Jimenez, J. T. Jayne and D. R. Worsnop, *ACS Earth Sp. Chem.*, 2018, **2**, 653–672.

38 S. Isokääntä, E. Kari, A. Buchholz, L. Hao, S. Schobesberger, A. Virtanen and S. Mikkonen, *Atmos. Meas. Tech.*, 2019, **13**, 2995–3022.

39 M. Takeuchi and N. L. Ng, *Atmos. Chem. Phys.*, 2019, **19**, 12749–12766.

40 G. Isaacman-Vanwertz, P. Massoli, R. OBrien, C. Lim, J. P. Franklin, J. A. Moss, J. F. Hunter, J. B. Nowak, M. R. Canagaratna, P. K. Misztal, C. Arata, J. R. Roscioli, S. T. Herndon, T. B. Onasch, A. T. Lambe, J. T. Jayne, L. Su, D. A. Knopf, A. H. Goldstein, D. R. Worsnop and J. H. Kroll, *Nat. Chem.*, 2018, **10**, 462–468.

41 K. H. Bates, T. B. Nguyen, A. P. Teng, J. D. Crounse, H. G. Kjaergaard, B. M. Stoltz, J. H. Seinfeld and P. O. Wennberg, *J. Phys. Chem. A*, 2016, **120**, 106–117.

42 B. H. Lee, F. D. Lopez-Hilfiker, C. Mohr, T. Kurtén, D. R. Worsnop, J. A. Thornton, T. Kurte, D. R. Worsnop, J. A. Thornton, T. Kurtén, D. R. Worsnop and J. A. Thornton, *Environ. Sci. Technol.*, 2014, **48**, 6309–6317.

43 P. S. Chhabra, A. T. Lambe, M. R. Canagaratna, H. Stark, J. T. Jayne, T. B. Onasch, P. Davidovits, J. R. Kimmel and D. R. Worsnop, *Atmos. Meas. Tech*, 2015, **8**, 1–18.

44 L. D. Yee, K. E. Kautzman, C. L. Loza, K. A. Schilling, M. M. Coggon, P. S. Chhabra, M. N. Chan, A. W. H. Chan, S. P. Hersey, J. D. Crounse, P. O. Wennberg, R. C. Flagan and J. H. Seinfeld, *Atmos. Chem. Phys*, 2013, **13**, 8019–8043.

45 L. Yu, J. Smith, A. Laskin, K. M. George, C. Anastasio, J. Laskin, A. M. Dillner and Q. Zhang, *Atmos. Chem. Phys.*, 2016, **16**, 4511–4527.

46 C. H. Clark, S. Nakao, A. Asa-Awuku, K. Sato and D. R. Cocker, *Aerosol Sci. Technol.*, 2013, **47**, 1374–1382.

47 S. Basnet, 2020.

48 T. Berndt, H. Herrmann, M. Sipilä and M. Kulmala, , DOI:10.1021/acs.jpca.6b10987.

49 E. L. D'ambro, B. H. Lee, J. Liu, J. E. Shilling, C. J. Gaston, F. D. Lopez-Hilfiker, S. Schobesberger, R. A. Zaveri, C. Mohr, A. Lutz, Z. Zhang, A. Gold, J. D. Surratt, J. C. Rivera-Rios, F. N. Keutsch and J. A. Thornton, *Atmos. Chem. Phys*, 2017, **17**, 159–174.

50 M. M. ¨ Uller, M. Graus, A. Wisthaler, A. Hansel, A. Metzger, J. Dommen and U. Baltensperger, *Atmos. Chem. Phys*, 2012, **12**, 829–843.

51 J. F. Hamilton, M. R. Alfarra, N. Robinson, M. W. Ward, A. C. Lewis, G. B. Mcfiggans, H. Coe and J. D. Allan, *Atmos. Chem. Phys*, 2013, **13**, 11295–11305.

52 D. O. De Haan, E. Tapavicza, M. Riva, T. Cui, J. D. Surratt, A. C. Smith, M.-C. Jordan, S. Nilakantan, M. Almodovar, T. N. Stewart, A. de Loera, A. C. De Haan, M. Cazaunau, A. Gratien, E. Pangui and O. Doussin, *Environ. Sci. Technol.*, 2018, **52**, 4061–4071.

53 R. H. Schwantes, K. A. Schilling, R. C. McVay, H. Lignell, M. M. Coggon, X. Zhang, P. O. Wennberg and J. H. Seinfeld, *Atmos. Chem. Phys.*, 2017, **17**, 3453–3474.

54 M. Brüggemann, L. Poulain, A. Held, T. Stelzer, C. Zuth, S. Richters, A. Mutzel, D. van Pinxteren, Y. Iinuma, S. Katkevica, R. Rabe, H. Herrmann and T. Hoffmann, *Atmos. Chem. Phys.*, 2017, **17**, 1453–1469.

55 M. Le Breton, M. Psichoudaki, M. Hallquist, Å. K. Watne, A. Lutz and Å. M. Hallquist, *Aerosol Sci. Technol.*, 2019, **53**, 244–259.

56 C. T. Cheng, M. N. Chan and K. R. Wilson, *J. Phys. Chem. A*, 2016, **120**, 5887–5896.

57 P. J. Gallimore, P. Achakulwisut, F. D. Pope, J. F. Davies, D. R. Spring and M. Kalberer, *Atmos. Chem. Phys.*, 2011, **11**, 12181–12195.

58 Y. B. Lim, Y. Tan, M. J. Perri, S. P. Seitzinger and B. J. Turpin, *Atmos. Chem. Phys.*, 2010, **10**, 10521–10539.

59 W. W. Hu, P. Campuzano-Jost, B. B. Palm, D. A. Day, A. M. Ortega, P. L. Hayes, J. E. Krechmer, Q. Chen, M. Kuwata, Y. J. Liu, S. S. de Sá, K. McKinney, S. T. Martin, M. Hu, S. H. Budisulistiorini, M. Riva, J. D. Surratt, J. M. St Clair, G. Isaacman-Van Wertz, L. D. Yee, A. H. Goldstein, S. Carbone, J. Brito, P. Artaxo, J. A. de Gouw, A. Koss, A. Wisthaler, T. Mikoviny, T. Karl, L. Kaser, W. Jud, A. Hansel, K. S. Docherty, M. L. Alexander, N. H. Robinson, H. Coe, J. D. Allan, M. R. Canagaratna, F. Paulot and J. L. Jimenez, *Atmos. Chem. Phys*, 2015, **15**, 11807–11833.

60 N. M. Donahue, A. Robinson, E. R. Trump, I. Riipinen and J. H. Kroll, *Top Curr Chem*, , DOI:10.1007/128_2012_355.

61 H. Zhang, L. D. Yee, B. H. Lee, M. P. Curtis, D. R. Worton, G. Isaacman-VanWertz, J. H. Offenberg, M. Lewandowski, T. E. Kleindienst, M. R. Beaver, A. L. Holder, W. A. Lonneman, K. S. Docherty, M. Jaoui, H. O. T. Pye, W. Hu, D. A. Day, P. Campuzano-Jost, J. L. Jimenez, H. Guo, R. J. Weber, J. De Gouw, A. R. Koss, E. S. Edgerton, W. Brune, C. Mohr, F. D. Lopez-Hilfiker, A. Lutz, N. M. Kreisberg, S. R. Spielman, S. V. Hering, K. R. Wilson, J. A. Thornton and A. H. Goldstein, *Proc. Natl. Acad. Sci.*, 2018, **115**, 2038–2043.

62 B. Wang and A. Laskin, *J. Geophys. Res. Atmos.*, 2014, **119**, 3335–3351.

63 M. M. Chim, C. T. Cheng, J. F. Davies, T. Berkemeier, M. Shiraiwa, A. Zuend and M. N. Chan, *Atmos. Chem. Phys.*, 2017, **17**, 14415–14431.

64 T. Berndt, N. Hyttinen, H. Herrmann and A. Hansel, , DOI:10.1038/s42004-019-0120-9.

65 C. Giorio, A. Monod, L. Brégonziobrégonzio-Rozier, H. L. Dewitt, M. Cazaunau, B. Temime-

Roussel, A. Gratien, V. Michoud, E. Pangui, S. Ravier, A. T. Zielinski, A. Tapparo, R. Vermeylen, M. Claeys, D. Voisin, M. Kalberer and J.-F. O. Doussin, *J. Phys. Chem. A*, 2017, **121**, 7641–7654.

66 K. Wang, 2018.

67 C. Mohr, F. D. Lopez-Hilfiker, P. Zotter, A. H. Preo, L. Xu, N. L. Ng, S. C. Herndon, L. R. Williams, J. P. Franklin, M. S. Zahniser, D. R. Worsnop, W. Berk Knighton, A. C. Aiken, K. J. Gorkowski, M. K. Dubey, J. D. Allan and J. A. Thornton, *Environ. Sci. Technol.*, 2013, **47**, 6316–6324.

68 M. Priestley, M. Le Breton, T. J. Bannan, K. E. Leather, A. Bacak, E. Reyes-Villegas, F. De Vocht, B. M. A. Shallcross, T. Brazier, M. Anwar Khan, J. Allan, D. E. Shallcross, H. Coe and C. J. Percival, *J. Geophys. Res. Atmos.*, 2018, **123**, 7687–7704.

69 A. P. Praplan, K. Hegyi-Gaeggeler, P. Barmet, L. Pfaffenberger, J. Dommen and U. Baltensperger, *Atmos. Chem. Phys*, 2014, **14**, 8665–8677.

70 A. Zaytsev, A. R. Koss, M. Breitenlechner, J. E. Krechmer, K. J. Nihill, C. Y. Lim, J. C. Rowe, J. L. Cox, J. Moss, J. R. Roscioli, M. R. Canagaratna, D. R. Worsnop, J. H. Kroll and F. N. Keutsch, *Atmos. Chem. Phys*, 2019, **19**, 15117–15129.

71 U. Molteni, F. Bianchi, F. Klein, I. El Haddad, C. Frege, M. J. Rossi, J. Dommen and U. Baltensperger, *Atmos. Chem. Phys*, 2018, **18**, 1909–1921.

72 Z. Finewax, J. A. De Gouw and P. J. Ziemann, *Environ. Sci. Technol.*, 2018, **52**, 1981–1989.

73 Y. Iinuma, E. Brüggemann, T. Gnauk, K. Müller, M. O. Andreae, G. Helas, R. Parmar and H. Herrmann, *J. Geophys. Res.*, 2007, **112**, D08209.

74 M. Busilacchio, P. Di Carlo, E. Aruffo, F. Biancofiore, C. D. Salisburgo, F. Giammaria, S. Bauguitte, J. Lee, S. Moller, J. Hopkins, S. Punjabi, S. Andrews, A. C. Lewis, M. Parrington, P. I. Palmer, E. Hyer and G. M. Wolfe, *Atmos. Chem. Phys*, 2016, **16**, 3485–3497.

75 E. Tsiligiannis, J. Hammes, C. M. Salvador, T. F. Mentel and M. Hallquist, *Atmos. Chem. Phys*, 2019, **19**, 15073–15086.

76 B. H. Lee, F. D. Lopez-Hilfiker, E. L. D'ambro, P. Zhou, M. Boy, T. Petäjä, L. Hao, A. Virtanen and J. A. Thornton, *Atmos. Chem. Phys*, 2018, **18**, 11547–11562.

77 P. S. Chhabra, A. T. Lambe, M. R. Canagaratna, H. Stark, J. T. Jayne, T. B. Onasch, P. Davidovits, J. R. Kimmel and D. R. Worsnop, *Atmos. Meas. Tech*, 2015, **8**, 1–18.

78 S. Schobesberger, H. Junninen, F. Bianchi, G. Lönn, M. Ehn, K. Lehtipalo, J. Dommen, S. Ehrhart, I. K. Ortega, A. Franchin, T. Nieminen, F. Riccobono, M. Hutterli, J. Duplissy, J. Almeida, A. Amorim, M. Breitenlechner, A. J. Downard, E. M. Dunne, R. C. Flagan, M. Kajos, H. Keskinen, J. Kirkby, A. Kupc, A. Kürten, T. Kurtén, A. Laaksonen, S. Mathot, A. Onnela, A. P. Praplan, L. Rondo, F. D. Santos, S. Schallhart, R. Schnitzhofer, M. Sipilä, A. Tomé, G. Tsagkogeorgas, H. Vehkamäki, D. Wimmer, U. Baltensperger, K. S. Carslaw, J. Curtius, A. Hansel, T. Petäjä, M. Kulmala, N. M. Donahue and D. R. Worsnop, *Proc. Natl. Acad. Sci. U. S. A.*, 2013, **110**, 17223–17228.

79 S. Kundu, R. Fisseha, A. L. Putman, T. A. Rahn and L. R. Mazzoleni, *Atmos. Chem. Phys.*, 2012, **12**, 5523–5536.

80 X. Zhang, R. C. Mcvay, D. D. Huang, N. F. Dalleska, B. Aumont, R. C. Flagan and J. H. Seinfeld, *Proc. Natl. Acad. Sci.*, 2015, **112**, 14168–14173.

81 L. Khachatryan, M. Barekati-Goudarzi, D. Kekejian, G. Aguilar, R. Asatryan, G. G. Stanley and D. Boldor, *Energy & Fuels*, 2018, **32**, 12597–12606.

82 Y. Huang, S. Qiu, I. N. Oduro, X. Guo and Y. Fang, , DOI:10.1021/acs.energyfuels.6b02250.

83 E. A. Dalluge, 2013.

84 J. F. Hamilton, M. R. Alfarra, K. P. Wyche, M. W. Ward, A. C. Lewis, G. B. Mcfiggans, N. Good, P. S. Monks, T. Carr, I. R. White and R. M. Purvis, *Atmos. Chem. Phys*, 2011, **11**, 5917–5929.

85 D. E. Romonosky, A. Laskin, J. Laskin and S. A. Nizkorodov, *J. Phys. Chem. A*, 2014, **119**, 2594–2606.

86 B. H. Lee, C. Mohr, F. D. Lopez-Hilfiker, A. Lutz, M. Hallquist, L. Lee, P. Romer, R. C. Cohen, S. Iyer, T. Kurten, W. Hu, D. A. Day, P. Campuzano-Jost, J. L. Jimenez, L. Xu, N. L. Ng, H. Guo, R. J. Weber, R. J. Wild, S. S. Brown, A. Koss, J. de Gouw, K. Olson, A. H. Goldstein, R. Seco, S. Kim, K. McAvey, P. B. Shepson, T. Starn, K. Baumann, E. S. Edgerton, J. Liu, J. E. Shilling, D. O. Miller, W. Brune, S. Schobesberger, E. L. D'Ambro and J. A. Thornton, *Proc. Natl. Acad. Sci. U. S. A.*, 2016, **113**, 1516–1521.

87 C. M. Boyd, J. Sanchez, L. Xu, A. J. Eugene, T. Nah, W. Y. Tuet, M. I. Guzman and N. L. Ng, *Atmos. Chem. Phys*, 2015, **15**, 7497–7522.

88 M. N. Chan, J. D. Surratt, A. W. H. Chan, K. Schilling, J. H. Offenberg, M. Lewandowski, E. O. Edney, T. E. Kleindienst, M. Jaoui, E. S. Edgerton, R. L. Tanner, S. L. Shaw, M. Zheng, E. M. Knipping and J. H. Seinfeld, *Atmos. Chem. Phys*, 2011, **11**, 1735–1751.

89 Y. Zhao, A. G. Hallar and L. R. Mazzoleni, *Atmos. Chem. Phys*, 2013, **13**, 12343–12362.